water

MDPI

Article

Mechanism and Quantitative Contribution Analysis of Pb(II) and Cd(II) Adsorption by Lignite Modified with *Phanerochaete chrysosporium*

Wenbo An [1,2,*], He Chen [1], Bin Xu [3], Tianzhi Wang [3], Guoxing Fu [1], Xiaowei Chen [1] and Qiqi Wang [4]

[1] School of Mechanical and Electrical Engineering, Hainan College of Software Technology, Qionghai 571400, China
[2] School of Mining Engineering, China University of Mining and Technology, Xuzhou 221000, China
[3] School of Civil Engineering, Liaoning Technical University, Fuxin 123000, China
[4] Qingyang Water Resources Comprehensive Affairs Center, Qingyang 745000, China
* Correspondence: wb_an1992@163.com

Abstract

To address the imbalance in aquatic ecosystems caused by lead and cadmium wastewater, this study proposes a novel approach using *Phanerochaete chrysosporium*-modified low-calorific lignite to prepare a lignite-based adsorbent (LBA) for efficient removal of Pb(II) and Cd(II) from wastewater. Through batch adsorption experiments, combined with kinetic, isotherm, and thermodynamic modeling, as well as multi-scale microscopic characterization techniques (BET, SEM-EDS, XRD, XPS, FTIR, and 2D-COS), the adsorption characteristics and mechanisms of LBA toward Pb(II) and Cd(II) were systematically investigated, and the quantitative contributions of each mechanism were analyzed. The results show that the optimal dosages of LBA for treating Pb(II) and Cd(II) wastewater are 0.4 g·L^{-1} and 1.3 g·L^{-1}, respectively. Under initial pH conditions of 4~6 and initial concentrations of 10 mg·L^{-1} (Pb(II)) and 3 mg·L^{-1} (Cd(II)), both heavy metal removal efficiency and equilibrium adsorption capacity reached their peak values. The adsorption processes fit well with the pseudo-second-order kinetic model and the Langmuir monolayer adsorption isotherm model, achieving maximum saturated adsorption capacities of 51.20 mg·g^{-1} (Pb(II)) and 57.34 mg·g^{-1} (Cd(II)). The adsorption of heavy metals on LBA is synergistically driven by four mechanisms—ion exchange, mineral precipitation, complexation with oxygen-containing functional groups, and π-electron coordination—among which complexation with oxygen-containing functional groups dominates (32.6%), followed by mineral precipitation (27.1%), π-electron coordination (23.4%), and ion exchange (16.9%). After three adsorption–desorption cycles, LBA still maintained over 70% removal efficiency for both Pb(II) and Cd(II), demonstrating excellent regeneration stability. In real automotive paint wastewater, removal rates for Pb(II), Cd(II), Cu(II), Zn(II), Fe(II), and Mn(II) all exceeded 83%, indicating strong practical applicability. Overall, the lignite-based adsorbent developed in this study exhibits outstanding adsorption performance and high potential for recyclability, offering a promising new technological pathway and theoretical foundation for treating lead- and cadmium-contaminated wastewater.

Keywords: lead and cadmium wastewater; lignite-based adsorbent; *Phanerochaete chrysosporium*; adsorption mechanism; quantitative contribution

Check for updates

Academic Editors: Li Ye and Ye Li

Received: 17 September 2026
Revised: 15 October 2026
Accepted: 26 October 2026
Published: 29 October 2026

Copyright: © 2026 by the authors. Licensee MDPI, Basel, Switzerland. This article is an open access article distributed under the terms and conditions of the Creative Commons Attribution (CC BY) license.

1. Introduction

In recent years, the continuous rise in global automotive demand has strongly driven the rapid development of the automotive industry. However, this expansion, while significantly increasing vehicle ownership, has also led to substantial emissions of toxic and hazardous substances into the environment. By 2024, the global number of motor vehicles, including passenger cars, trucks, and buses, had reached approximately 1.705 billion, a marked increase from 700 million in 2000. Taking a typical automobile manufacturing plant with an annual production capacity of 400,000 vehicles as an example, it generates about 410,000 cubic meters of wastewater annually, primarily from key processes such as machining, forming, welding, surface treatment, painting, and final assembly [1]. This wastewater contains various toxic and harmful components, including paint ingredients, heavy metals, phosphates, particulate matter (PM), chemical oxygen demand (COD), biochemical oxygen demand (BOD), surfactants, petroleum hydrocarbons, and lubricants [2,3]. Among these, heavy metals such as chromium (Cr), cadmium (Cd), lead (Pb), and nickel (Ni) pose particularly significant environmental risks. Lead and cadmium are especially concerning due to their high toxicity even at extremely low concentrations and their non-biodegradability; they are widely recognized as the two most dangerous heavy metal pollutants to human health and are among the most commonly detected heavy metals in aquatic ecosystems [4,5]. Wastewater containing lead and cadmium exhibits unique ecological risk characteristics: its high toxicity and persistence result in long-term accumulation in the environment and facilitate biomagnification through the food chain, ultimately posing serious threats to human health [6]. Moreover, these metals can exert strong selective toxic effects on specific cells or organs [7]. According to the World Health Organization (WHO) Guidelines for Drinking-Water Quality and China's Integrated Wastewater Discharge Standard (GB 8978-1996), the maximum allowable concentrations of Pb(II) and Cd(II) in drinking water are 0.01 mg·L^{-1} and 0.003 mg·L^{-1}, respectively, while the discharge limits for wastewater are 1.0 mg·L^{-1} and 0.1 mg·L^{-1}, respectively. Given the current pollution situation and these stringent standards, developing efficient, environmentally friendly, and economically viable technologies for treating lead- and cadmium-containing wastewater has become an urgent necessity.

Various treatment technologies have been developed for managing lead- and cadmium-containing wastewater [8–10], broadly categorized into physicochemical methods (e.g., adsorption), advanced oxidation processes (e.g., photocatalysis), and electrochemical approaches (e.g., electrodialysis). Among these, adsorption is the most widely used method due to its simplicity and high removal efficiency [11]. However, commonly used adsorbents, such as activated carbon [12], zeolites [13], and oyster shells [14,15], typically face limitations, including high cost, insufficient equilibrium adsorption capacity, and poor regeneration performance. In recent years, innovative adsorbents, including biochar, metal–organic frameworks (MOFs) and graphene-based aerogels (GBAs), have attracted widespread attention, yet some bottlenecks still restrict their practical applications [16]. Therefore, developing novel adsorbents that are low-cost, highly efficient, and environmentally compatible has become a major research focus in this field.

Lignite is a naturally low-grade coal type with relatively low calorific value, but it features high porosity and a large specific surface area. Its surface is rich in functional groups such as carboxyl, carbonyl, and hydroxyl groups, which can act as active sites for ion exchange and coordination adsorption of heavy metal ions, making it an ideal precursor for preparing adsorbent materials [17,18]. Studies have shown that lignite can effectively adsorb various organic and inorganic pollutants from aqueous solutions [19]. However, the equilibrium adsorption capacity of raw lignite is relatively limited, and its selectivity toward target heavy metal ions remains unsatisfactory. To overcome these

limitations, physical, chemical, or biological modification strategies, such as acid treatment, oxidation, or loading with nanomaterials, can be employed to tailor pore structure, enrich surface functional groups, and activate adsorption sites [20,21]. Although both physical and chemical modifications have been proven effective in enhancing lignite's equilibrium adsorption capacity, they each face significant practical constraints: physical modification typically requires stringent reaction equipment and operating conditions, while chemical modification may introduce secondary pollution risks due to reagent use (e.g., emissions of exhaust gases and generation of waste liquids). In contrast, biological modification leverages the metabolic and transformation capabilities of fungi, bacteria, and actinomycetes to achieve targeted structural adjustment and performance optimization of lignite, offering distinct advantages including mild reaction conditions, environmental friendliness, and remarkable effectiveness [22,23].

Based on this, the present study aims to further introduce biological modification methods following acid–base pretreatment. Acid–base treatment can significantly increase the specific surface area of lignite and enhance the number of active sites, while subsequent biological modification is expected to synergistically improve its adsorption selectivity and capacity. To date, several microorganisms with high-efficiency lignite-degrading capabilities have been screened, among which white-rot fungi, *Phanerochaete chrysosporium*, and Penicillium species stand out [24]. These strains secrete extracellular enzyme systems capable of specifically modifying the macromolecular structure of lignite [25,26]. Klein et al. [27] investigated the growth-promoting and detoxifying effects of a bioagent prepared from the culture broth of white-rot basidiomycetes in the biodesulfurization process of lignite, finding that fungal degradation activity mainly results from the synergistic catalytic action of lignin-degrading enzymes such as manganese peroxidase and lignin peroxidase. Yin et al. [28] reported that after nitric acid pretreatment, the biodegradation rate of lignite reached 31.83% within 11 days; other studies also showed that the degradation efficiency of pretreated coal samples typically ranged between 7% and 32% over two weeks. *Phanerochaete chrysosporium* is considered among the most effective lignin-degrading microorganisms in nature, and its secreted extracellular enzymes, including laccase, manganese peroxidase, lignin peroxidase, and versatile peroxidase, play crucial roles in lignin degradation [29,30]. White-rot fungus modification was selected to regulate the surface functional groups of lignite because it is an eco-friendly and mild biological route that avoids the use of corrosive chemical reagents [31]. However, to date, there has been limited research on using white-rot fungi to modify lignite for preparing biochar or systematically investigating the adsorption mechanisms of Pb(II) and Cd(II) via such biochar in lead–cadmium-containing wastewater, leaving this area ripe for further exploration. In addition, unlike most previous lignite and biochar studies that only qualitatively interpret adsorption mechanisms, this work quantifies the contribution proportion of each heavy metal removal pathway. This quantitative mechanistic analysis provides deeper insights into heavy metal immobilization using fungus-modified lignite materials.

This study selected lignite as the substrate and employed a *Phanerochaete chrysosporium* biomodification process to prepare a lignite-based adsorbent (LBA), systematically evaluating its adsorption efficiency for Pb(II) and Cd(II) in simulated wastewater containing lead and cadmium. Through batch adsorption experiments, combined with adsorption kinetics, isotherm models, and thermodynamic parameter calculations, the adsorption behavior was analyzed. Utilizing microscopic characterization techniques, such as BET, SEM-EDS, XRD, FTIR, 2D-COS, and XPS, the research further revealed the morphological evolution, functional group transformations, and pore structure responses before and after adsorption, thereby elucidating the underlying mechanisms and calculating the contribution rates of each mechanism. Overall, this study not only provides a sustainable adsorbent material

solution for treating lead- and cadmium-containing wastewater in the automotive manufacturing industry but also opens up a feasible technological pathway for the functional transformation of low-rank lignite.

2. Materials and Methods

2.1. Source of the Strain and Culture Method

The standard strain of *Phanerochaete chrysosporium* (designated NDM3-2, second-generation subculture, preserved on agar slants) used in this study was obtained from the China Industrial Microbial Culture Collection Center (CICC, Beijing, China). Under aseptic conditions in a laminar flow hood, a sterile inoculation loop was used to transfer a small amount of mycelium from the slant culture into potato dextrose broth (PDB). The PDB medium was prepared as follows: 300 g of peeled, fresh potatoes were cut into small pieces, suspended in 1 L of deionized water, and boiled for 30 min; the mixture was then filtered through sterile gauze, and the resulting filtrate was supplemented with 20 g of glucose. The final volume was adjusted to 1 L with deionized water, and the medium was sterilized by autoclaving at 121 °C for 20 min. The inoculated PDB cultures were incubated statically in a biochemical incubator at 35 ± 1 °C for 48 h.

2.2. Preparation of Lignite-Based Adsorbent

The coal samples employed in this study were sourced from the Ordos Basin, Inner Mongolia Autonomous Region, China. Raw coal was subjected to mechanical comminution, followed by grinding and sieving to achieve a uniform particle size distribution. LBA was prepared based on preliminary screening experiments. The detailed preparation procedures are described as follows. The coal was treated with 5 mol/L nitric acid (HNO_3) for 48 h under static conditions. After acid treatment, the sample was thoroughly washed with deionized water until the filtrate reached neutral pH (pH ≈ 7). The washed material was then dried in a forced-air oven at 60 °C to constant weight, cooled to ambient temperature in a desiccator, and stored in an airtight container under inert conditions. For biofunctionalization, the dried lignite was mixed with PDB medium at a predetermined solid-to-liquid ratio and sterilized by autoclaving at 121 °C and 103 kPa for 30 min using an XFH-50CA autoclave (Xinhua Medical Instrument Co., Ltd., Hangzhou, China). Following sterilization, the mixture was allowed to cool passively to room temperature (25 ± 1 °C) under aseptic conditions. Thereafter, a 48 h old actively growing culture of a pre-activated *Phanerochaete chrysosporium* strain was inoculated into the sterile medium inside a Class II biological safety cabinet (VD-650, Suzhou Purifier Equipment Co., Ltd., Suzhou, China). The inoculated flasks were incubated in a temperature-controlled orbital shaker incubator maintained at 30 ± 1 °C for 13 days. Upon completion of incubation, the reaction mixture was vacuum-filtered, and the resulting solid residue was centrifuged (8000× *g*, 10 min) to separate fungal mycelia. The supernatant was discarded, and the pellet was repeatedly washed with deionized water to remove residual biomass and soluble metabolites. The purified solid product was dried at 60 °C to constant weight, yielding the final lignite-based adsorbent (LBA). The synthesis procedure of LBA is shown in Figure S1. The dried adsorbent was subsequently sieved to retain particles within the 60~80 mesh range, stored, and desiccated at room temperature pending characterization and application.

2.3. Batch Adsorption Experiment

Table S1 summarizes the experimental design parameters for the adsorption studies. All adsorption experiments were carried out under controlled oscillation at 125 rpm for a contact time of 720 min. Upon completion of adsorption, aliquots were filtered through 0.22 μm polyethersulfone (PES) membrane filters, and the equilibrium concentrations

of Pb(II) and Cd(II) in the filtrates were quantified using flame atomic absorption spectrophotometry (FAAS), following the procedures specified in GB/T 7475–1987; Water quality—Determination of copper, zinc, lead and cadmium—Atomic absorption spectrometry. Standards Press of China: Beijing, China, 1987.. Calibration curves for Pb(II) and Cd(II) were constructed from standard solutions spanning appropriate concentration ranges ($R^2 \geq 0.999$), and all measurements were performed in triplicate to ensure analytical reproducibility. Removal rate (R_e, %) and adsorption capacity (q_e, mg·g^{-1}) were calculated according to standard equations.

Kinetic adsorption behavior was evaluated using three classical models: the pseudo-first-order model (PFO), the pseudo-second-order model (PSO), and the Weber–Morris intra-particle diffusion model (IPD). Equilibrium adsorption isotherms were fitted to both the Langmuir and Freundlich models. Both kinetic and isotherm models were processed via non-linear regression rather than linearized transformation. Root-mean-square error (RMSE) was used as the error function for fitting optimization, and the coefficient of determination R^2 was calculated to evaluate model goodness-of-fit. The corresponding mathematical expressions are provided in Text S1 of the Supplementary Materials.

2.4. Adsorption–Desorption Experiment

Desorption experiments were conducted on LBA materials loaded with Pb(II) and Cd(II) (denoted as LBA-Pb(II) and LBA-Cd(II)) using five desorbing agents: 1.0 mol·L^{-1} HCl, 0.1 mol·L^{-1} HCl, 1.0 mol·L^{-1} NaOH, 0.1 mol·L^{-1} NaOH, and deionized water. Specifically, equal amounts of LBA-Pb(II) or LBA-Cd(II) samples were mixed with 50 mL of the corresponding desorbing agent and shaken at 125 rpm for 12 h. Afterward, the mixtures were centrifuged, separated, and dried. The adsorption–desorption cycle was repeated 5 times to systematically evaluate the regeneration efficiency and structural stability of the LBA material under different desorption conditions.

2.5. Characterization

Sample morphology was examined using an ultra-high-resolution cold-field-emission scanning electron microscope (FE-SEM, JEOL JSM-7610Plus, Tokyo, Japan) operated at an accelerating voltage of 5 kV and a working distance of 8 mm. Specific surface area, total pore volume, and average pore diameter were determined by nitrogen physisorption at 77 K using an automated surface area and porosimetry analyzer (BET, Micromeritics ASAP 2020; Micromeritics Instrument Corp., Norcross, GA, USA). Crystalline phase identification was performed via X-ray diffraction (XRD, Bruker D8 ADVANCE; Bruker AXS GmbH, Karlsruhe, Germany) with a Cu Kα radiation source (λ = 1.5418 Å), operating at 40 kV and 40 mA, with a scan range of 10°~80° (2θ) and a step size of 0.02°. Functional group analysis was conducted by Fourier-transform infrared spectroscopy (FTIR, Thermo Scientific Nicolet iS50; Thermo Fisher Scientific Inc., Madison, WI, USA), collecting spectra in transmission mode across 4000~400 cm^{-1} at a spectral resolution of 4 cm^{-1} and averaging 64 co-added scans. Surface elemental composition and chemical state information were acquired by X-ray photoelectron spectroscopy (XPS, Thermo Scientific ESCALAB 250Xi; Thermo Fisher Scientific Inc., Loughborough, UK) employing a monochromated Al Kα X-ray source ($h\nu$ = 1486.6 eV); binding energies were calibrated to the C1s peak at 284.8 eV for charge referencing.

2.6. Contribution of Different Adsorption Mechanisms

The demineralized adsorbent (LBA_{dem}) was prepared by treating the as-synthesized lignite-based adsorbent (LBA) with 1 mol·L^{-1} HCl under reflux for 2 h, followed by thorough washing with deionized water until the filtrate reached neutral pH and drying at 60 °C

under vacuum. Batch adsorption experiments were conducted on both LBA and LBAdem using an initial Pb(II)/Cd(II) concentration of 400 mg·L^{-1} and an adsorbent dosage of 2 g·L^{-1} at 25 ± 1 °C, with agitation at 125 rpm for 12 h. The contributions of four distinct adsorption mechanisms (mineral precipitation (Q_p), ion exchange (Q_e), surface functional group chelation (Q_f), and π-electron coordination (Q_π)) were quantitatively deconvoluted based on mass balance and complementary characterization data. The calculation of the contribution of each mechanism is described in detail in references [32,33].

(1) Ion Exchange: Q_e

The ion-exchange contribution was calculated by charge equivalents:

$$n_{eq} = z \times n.$$

where n_{eq} is the charge equivalent of each released cation (mol); z represents the cation valence; and n is the molar amount of released K^+, Na^+, Ca^{2+}, Mg^{2+} (mol).

The total charge equivalents released from LBA surface cations were summed. According to charge balance, the molar amount of divalent heavy metal ions removed via ion exchange:

$$n_{metal} = n_{eq,total}/2.$$

The ion-exchange adsorption capacity Q_e (mg·g^{-1}) was determined by multiplying n_{metal} by the molar mass of Pb(II) or Cd(II).

(2) Mineral Precipitation:

$$Q_p = Q_t - Q_a - Q_e$$

where Q_t is the total adsorption capacity (mg·g^{-1}), Q_a is the adsorption capacity of LBAdem (mg·g^{-1}), and Q_p is the adsorption capacity of mineral precipitation (mg·g^{-1}).

(3) Surface Functional Group Chelation: H^+ is released during the complexation of Pb(II) and Cd(II) with oxygen-containing functional groups on the surface of the adsorbent, resulting in a change in the pH of the solution, so the amount of Pb(II) and Cd(II) adsorbed by the complexation can be calculated from the change in pH:

$$Q_f = Q_{pH}$$

where Q_{pH} is the amount of Pb(II) and Cd(II) adsorbed by the complexation of oxygen-containing functional groups of LBAdem (mg·g^{-1}).

(4) Coordination with π-electrons:

$$Q_\pi = Q_a - Q_f$$

2.7. Quality Assurance/Quality Control

All chemical reagents were of analytical purity (≥99.0%) and purchased from Shanghai Aladdin Biotechnology Co., Ltd. Shanghai, China. Deionized water was used for all solution preparations and rinsing procedures. Glassware was successively soaked in 5% (v/v) HNO_3 solution for 24 h, ultrasonically cleaned (30 min), repeatedly rinsed with deionized water until neutral, and then dried at a constant temperature of 105 °C for storage. Pb(II) and Cd(II) standard stock solutions (1000 mg·L^{-1}) were precisely prepared by weighing high-purity $Pb(NO_3)_2$ and $Cd(NO_3)_3{\cdot}4H_2O$. The metal solutions used in batch experiments were obtained by successive dilution of the stock solutions. pH was adjusted by adding 0.1 mol·L^{-1} HCl or 0.1 mol·L^{-1} NaOH. Three independent parallel samples were set for each group of experiments, and blank samples were run simultaneously to correct for background interference. All concentration determination results were reported based on the arithmetic mean of three repeated measurements, with the relative standard deviation (RSD) controlled within ≤5.0%.

3. Results and Discussion

3.1. Characterization of LBA

The N_2 adsorption–desorption isotherms of raw lignite (Figure 1a) and LBA (Figure 1b) both conform to the characteristics of Type IV isotherms according to IUPAC classification [34], exhibiting hysteresis loops at relative pressures $P/P_0 > 0.4$, indicating that both materials possess mesoporous structures. As P/P_0 approaches 1.0, the saturated adsorption capacity of raw lignite is only about 6.5 $cm^3 \cdot g^{-1}$ (STP), reflecting severely underdeveloped porosity; in contrast, LBA achieves a saturated adsorption capacity of 130 $cm^3 \cdot g^{-1}$ (STP), nearly 20 times higher than that of raw lignite, confirming that microbial metabolic activity can significantly reconstruct the pore system of lignite. In the low-pressure region ($P/P_0 < 0.1$), corresponding to monolayer adsorption dominated by micropores, the adsorption curve of raw lignite rises gently, indicating extremely limited micropore content, whereas LBA shows a marked steep increase, suggesting that microbial activity has induced the formation of abundant micropores, thereby greatly enhancing its specific surface area. In the medium-to-high pressure range ($0.4 < P/P_0 < 0.8$), the adsorption and desorption branches of raw lignite are widely separated with a broad hysteresis loop, indicating that its native mesopores are predominantly isolated and closed, with poor connectivity; in comparison, the hysteresis loop of LBA is significantly narrowed, with adsorption and desorption curves highly overlapping, reflecting that microbes have effectively opened blocked pores by dissolving inorganic mineral components and degrading organic cementing materials, thus improving pore connectivity [35]. In the high-pressure region ($0.8 < P/P_0 < 1.0$), both samples experience a sharp rise in adsorption due to capillary condensation within large mesopores/macropores; however, the increase in LBA is significantly greater than that of raw lignite, further demonstrating the development of a multi-level porous structure featuring coordinated distributions of micropores, mesopores, and macropores.

The BJH pore size distribution curves (Figure 1c,d) further confirm the aforementioned pore evolution patterns: the pore volumes of raw lignite and LBA are predominantly concentrated in the micropores and small mesopores ranging from 0 to 10 nm, while macropores above 10 nm contribute negligibly to the total pore volume. The peak pore volume density of raw lignite is only 0.0048 $cm^3 \cdot g^{-1} \cdot nm^{-1}$, with almost no effective pore volume response below 2 nm, consistent with its low nitrogen adsorption capacity and limited monolayer adsorption sites, as indicated by the isotherm characteristics. In contrast, the peak pore volume density of LBA increases significantly to 0.033 $cm^3 \cdot g^{-1} \cdot nm^{-1}$ (approximately sevenfold), featuring a distinct sharp peak in the micropore region below 2 nm, directly confirming that microbial degradation of the dense coal macromolecular framework induces deep etching and generates abundant micropores. Meanwhile, the pore volume density in the small mesopore range of 2~6 nm also shows a marked increase, indicating that originally isolated mesopores have been activated through expansion and connectivity enhancement. Furthermore, LBA still exhibits detectable, albeit weak, pore volume contributions in the 10~50 nm range, corroborating the stronger capillary condensation signals observed at high pressures in the isotherms.

The BET specific surface area and BJH pore size distribution analyses collectively indicate that microorganisms, by selectively dissolving inorganic mineral phases within the coal matrix and degrading organic cementing components, not only generate a large number of micropores but also significantly enhance the connectivity and openness of the mesoporous network. This ultimately leads to the synergistic development of micropores and small mesopores, establishing a well-developed, multi-level porous system characterized by high specific surface area, high total pore volume, and multi-scale interconnectivity. This conclusion is further supported by scanning electron microscopy (SEM) morphology observations: the raw lignite (Figure 1e) exhibits a dense and smooth surface with only scattered,

shallow, isolated pores, lacking densely packed nanoscale pores; in contrast, the LBA matrix (Figure 1f) shows obvious fragmentation and loosening, with uniformly distributed high-density nanopores on the surface and multiple interconnected large mesopores forming cavities, resulting in significantly enhanced overall pore openness and structural complexity.

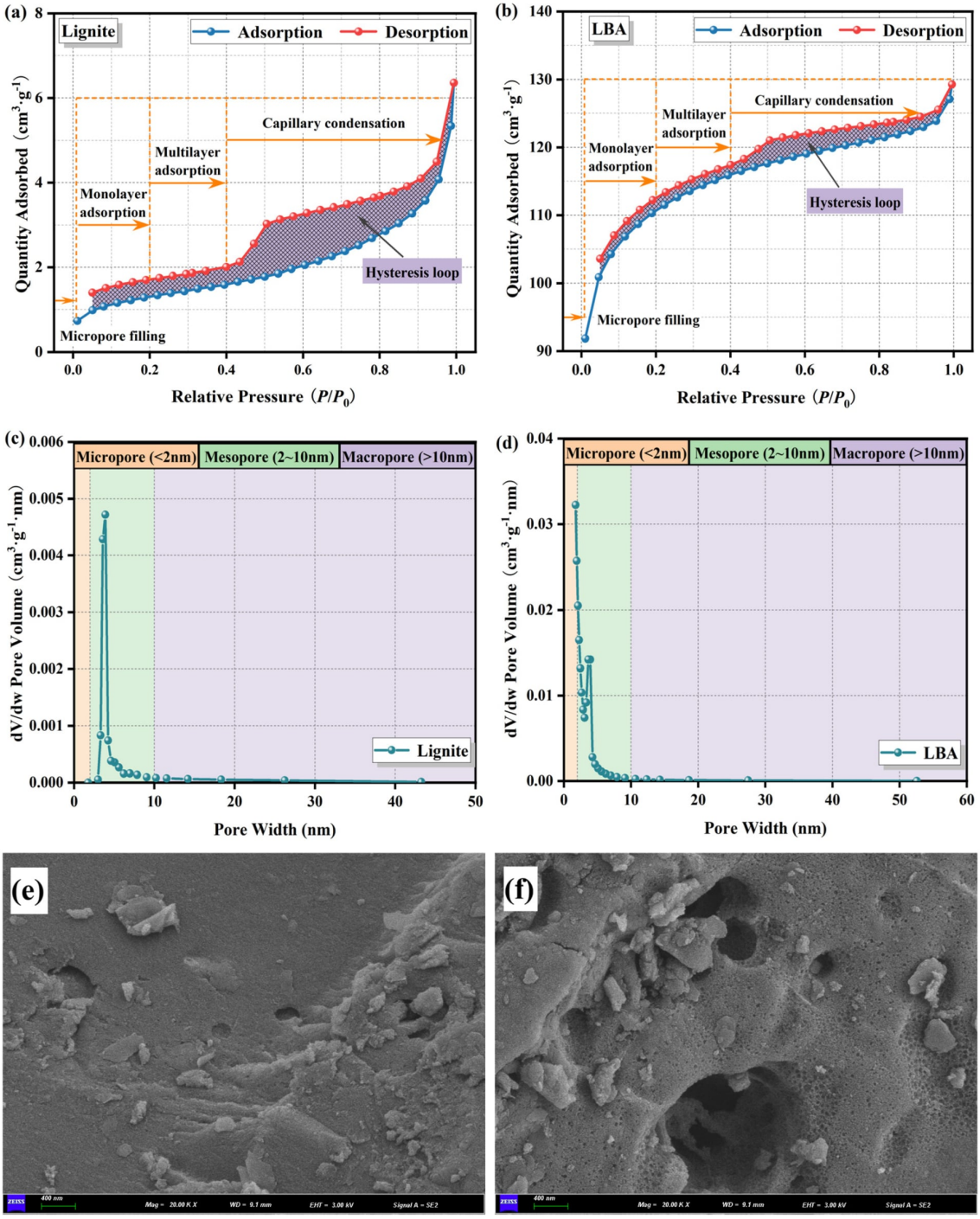


Figure 1. Characterization of lignite and LBA. (**a**) N_2 adsorption–desorption isotherm of lignite. (**b**) N_2 adsorption–desorption isotherm of LBA. (**c**) Pore diameter distribution of lignite. (**d**) Pore diameter distribution of LBA. (**e**) SEM of lignite. (**f**) SEM of LBA.

3.2. Batch Adsorption Experiments

Figure 2a illustrates the influence of LBA dosage on the adsorption efficiency of Pb(II) and Cd(II). As the LBA dosage increases, the removal efficiency of both metal ions improves

progressively, primarily due to the greater availability of active adsorption sites. However, beyond a certain threshold, excessive LBA dosage induces particle aggregation, leading to a decline in effective specific surface area and an increase in liquid–solid interfacial mass transfer resistance, both of which impede adsorption kinetics and reduce overall process efficiency. To balance adsorption performance, operational cost, and sustainability considerations, including energy consumption and environmental footprint, the optimal dosages were determined as 0.4 g for Pb(II) removal and 1.3 g for Cd(II) removal.

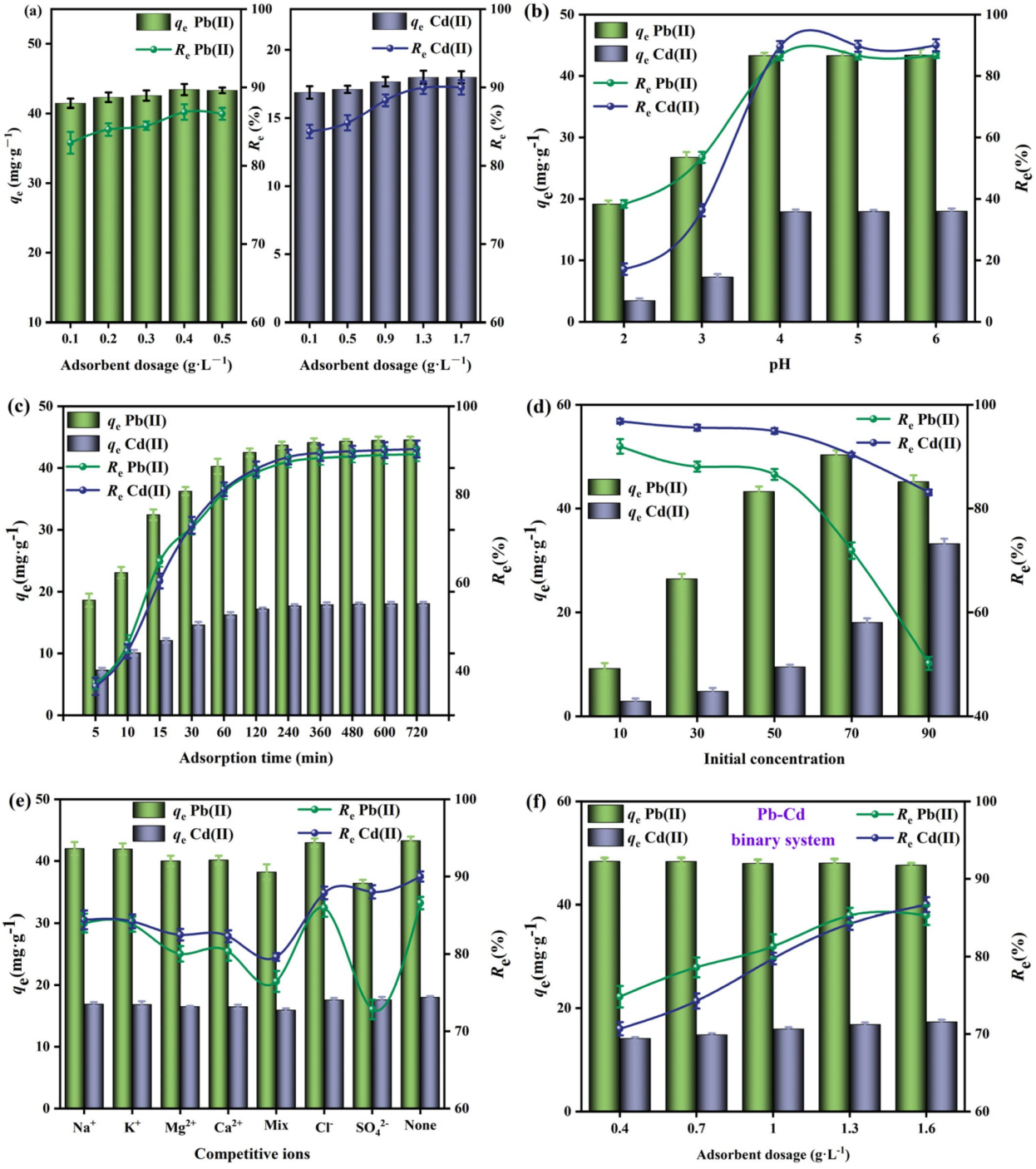


Figure 2. Batch adsorption experiments of LBA. (**a**) Adsorbent dosage. (**b**) pH. (**c**) Adsorption time. (**d**) Initial concentration. (**e**) Competitive ions. (**f**) Pb-Cd binary system.

Figure 2b depicts the influence of solution pH on the adsorption efficiency of Pb(II) and Cd(II). Over a pH range of 2~6, both the removal efficiency and equilibrium adsorption capacity for Pb(II) and Cd(II) exhibit a marked upward trend with increasing pH. This behavior is governed by the protonation–deprotonation equilibria of oxygen-containing functional groups, particularly carboxyl (–COOH) and phenolic hydroxyl (–OH) groups, on the LBA surface. At highly acidic pH (<4), these groups remain predominantly protonated, conferring a net positive surface charge to LBA. Consequently, electrostatic repulsion between the positively charged surface and cationic metal species (Pb(II)/Cd(II)) occurs, while, simultaneously, abundant H^+ ions in solution competitively occupy more than 80% of the anionic binding sites, substantially suppressing metal ion adsorption [36]. In contrast, as pH rises to 4~6, progressive deprotonation leads to a net negative surface charge. H^+ competition diminishes markedly, and deprotonated sites, primarily $–COO^-$ and phenolate $–O^-$, become available to engage Pb(II) and Cd(II) via combined electrostatic attraction and inner-sphere coordination, thereby significantly enhancing adsorption performance [37]. Accordingly, the pH range of 4~6 is identified as the optimal operational window for efficient adsorption of both metals.

Figure 2c illustrates the time-dependent adsorption kinetics of Pb(II) and Cd(II) onto LBA. The adsorption process follows a characteristic biphasic profile: an initial rapid phase followed by a gradual approach to equilibrium. Within the first 15 min, removal efficiency rises sharply, driven primarily by a steep concentration gradient and the availability of abundant, unoccupied surface binding sites. Between 15 and 120 min, the adsorption rate decelerates progressively as active sites become increasingly occupied, and intra-particle diffusion resistance intensifies. Beyond 120 min, adsorption reaches pseudo-equilibrium; further uptake is impeded by near-complete site saturation and the development of electrostatic repulsion arising from localized positive surface charge accumulation, both thermodynamically and kinetically limiting additional metal ion binding.

Figure 2d illustrates the influence of initial Pb(II) and Cd(II) concentrations on the adsorption performance of LBA. With increasing initial metal ion concentration, the removal efficiency for both ions declines, whereas the equilibrium adsorption capacity increases progressively. This inverse relationship arises from competing mass transfer and surface saturation effects: at low initial concentrations, abundant unoccupied active sites enable rapid ion diffusion and efficient interfacial contact, yielding high removal efficiencies; at elevated concentrations, the steeper chemical potential gradient intensifies the thermodynamic driving force for adsorption, enhancing ion flux toward the surface and promoting greater uptake per unit mass of adsorbent [38]. Nevertheless, as adsorption proceeds, site occupancy rises, eventually approaching saturation; under excess metal loading, surface charge reversal (from negative to positive) occurs, compressing the electrical double layer and generating electrostatic repulsion that impedes further ion approach and binding, thus limiting removal efficiency. Therefore, initial concentration, as a key driving force for mass transfer, can to some extent overcome mass transfer resistance at the adsorption interface, particularly under high-concentration conditions; a stronger chemical potential gradient effectively promotes the migration and enrichment of Pb(II) and Cd(II) from the aqueous phase to the solid phase [39].

Figure 2e illustrates the influence of coexisting ions on the adsorption of Pb(II) and Cd(II) by LBA. In multicomponent systems, background divalent cations, particularly Ca^{2+} and Mg^{2+}, substantially suppress the removal efficiency of both target metals. This competitive behavior arises from the combined effects of charge density, hydration energy and hydrated ionic radius. They compete with heavy metal cations for available negatively charged surface sites on LBA. In contrast, SO_4^{2-} exerts ion-specific effects: for Pb(II), it induces heterogeneous precipitation of sparingly soluble $PbSO_4$ ($K_{sp} = 1.6 \times 10^{-8}$),

thereby inflating the apparent removal efficiency, a contribution distinct from true surface adsorption; for Cd(II), however, the high solubility of $CdSO_4$ ($K_{sp} = 1.5 \times 10^{-5}$) precludes significant precipitate formation, resulting in negligible interference with the intrinsic adsorption mechanism.

Figure 2f further reveals the adsorption characteristics in the Pb(II)-Cd(II) binary system. Under identical LBA dosing conditions, the removal efficiencies of both ions are lower than their respective values in single-metal systems, primarily due to increased total metal ion load and direct competition between Pb(II) and Cd(II) for adsorption sites. Notably, Pb(II) exhibits higher adsorption priority, closely related to its smaller hydrolysis constant ($K_{h,Pb} = 7.8 < K_{h,Cd} = 9.2$) and smaller hydrated radius (0.401 nm < 0.426 nm), which facilitate easier dehydration and closer approach to adsorption sites, thereby promoting coordination exchange or ion exchange processes [40]. Furthermore, thermodynamic analysis (Table S5) indicates that at the same temperature, the Gibbs free energy change (ΔG) for Pb(II) adsorption by LBA is more negative, confirming a stronger thermodynamic spontaneity compared to Cd(II), thus supporting the preferential adsorption mechanism of Pb(II). As LBA dosage increases from 0 to 2.0 $g \cdot L^{-1}$, the removal rates of both Pb(II) and Cd(II) show an upward trend. At low dosages (<0.5 $g \cdot L^{-1}$), limited active sites are predominantly occupied by Pb(II), which has higher adsorption affinity; when the dosage exceeds 1.0 $g \cdot L^{-1}$, sufficient adsorption sites become available, and residual Pb(II) concentration in solution significantly decreases, providing Cd(II) with more binding opportunities, leading to improved removal efficiency until it eventually stabilizes.

3.3. Adsorption Characteristics

3.3.1. Adsorption Kinetics

The fitting results of the kinetics experiments for the adsorption of Pb(II) and Cd(II) onto LBA are shown in Table S2 and Figure 3a. The PSO kinetic model provided a significantly better fit to the adsorption process of Pb(II) and Cd(II) on LBA compared to the PFO kinetic model, with relative errors between the calculated equilibrium adsorption capacity ($q_{e,cal}$) and experimental values ($q_{e,exp}$) all below 0.8%, confirming that this model more accurately describes the rate-controlling mechanism [41]. According to the pseudo-second-order kinetic theory, the adsorption rate is proportional to the square of the concentration of unoccupied active sites on the adsorbent surface, indicating that chemical adsorption dominates the process, involving surface complexation reactions with electron sharing or transfer [42]. The IPD model fitting results (Figure 3b) revealed that the adsorption process of Pb(II) and Cd(II) onto LBA can be clearly divided into three consecutive stages: the first stage is rapid surface adsorption dominated by film diffusion, characterized by high initial diffusion rate constants ($K_{31,Pb} = 8.2958$ $mg \cdot g^{-1} \cdot min^{-0.5}$; $K_{31,Cd} = 2.1766$ $mg \cdot g^{-1} \cdot min^{-0.5}$); the second stage involves an increasing contribution from intra-particle diffusion, reflecting growing resistance to ion migration into micropores/mesopores ($K_{32,Pb} = 1.3669$ $mg \cdot g^{-1} \cdot min^{-0.5}$; $K_{32,Cd} = 0.4964$ $mg \cdot g^{-1} \cdot min^{-0.5}$); and the third stage approaches equilibrium, indicating a significant reduction in mass transfer driving force ($K_{33,Pb} = 0.1102$ $mg \cdot g^{-1} \cdot min^{-0.5}$; $K_{33,Cd} = 0.0495$ $mg \cdot g^{-1} \cdot min^{-0.5}$). The boundary layer thickness follows the order $C_1 < C_2 < C_3$, suggesting that the boundary layer continuously thickens as the reaction progresses, hindering the diffusion of Pb(II) and Cd(II) toward LBA and causing the adsorption process to increasingly deviate from the IPD model. Notably, none of the three fitted lines pass through the origin, and their deviations become progressively larger, indicating that, in addition to intra-particle diffusion, both liquid-film diffusion in the boundary layer and surface adsorption potential field also contribute to the rate control, consistent with the characteristics of multi-scale mass transfer coupling mechanisms [43].

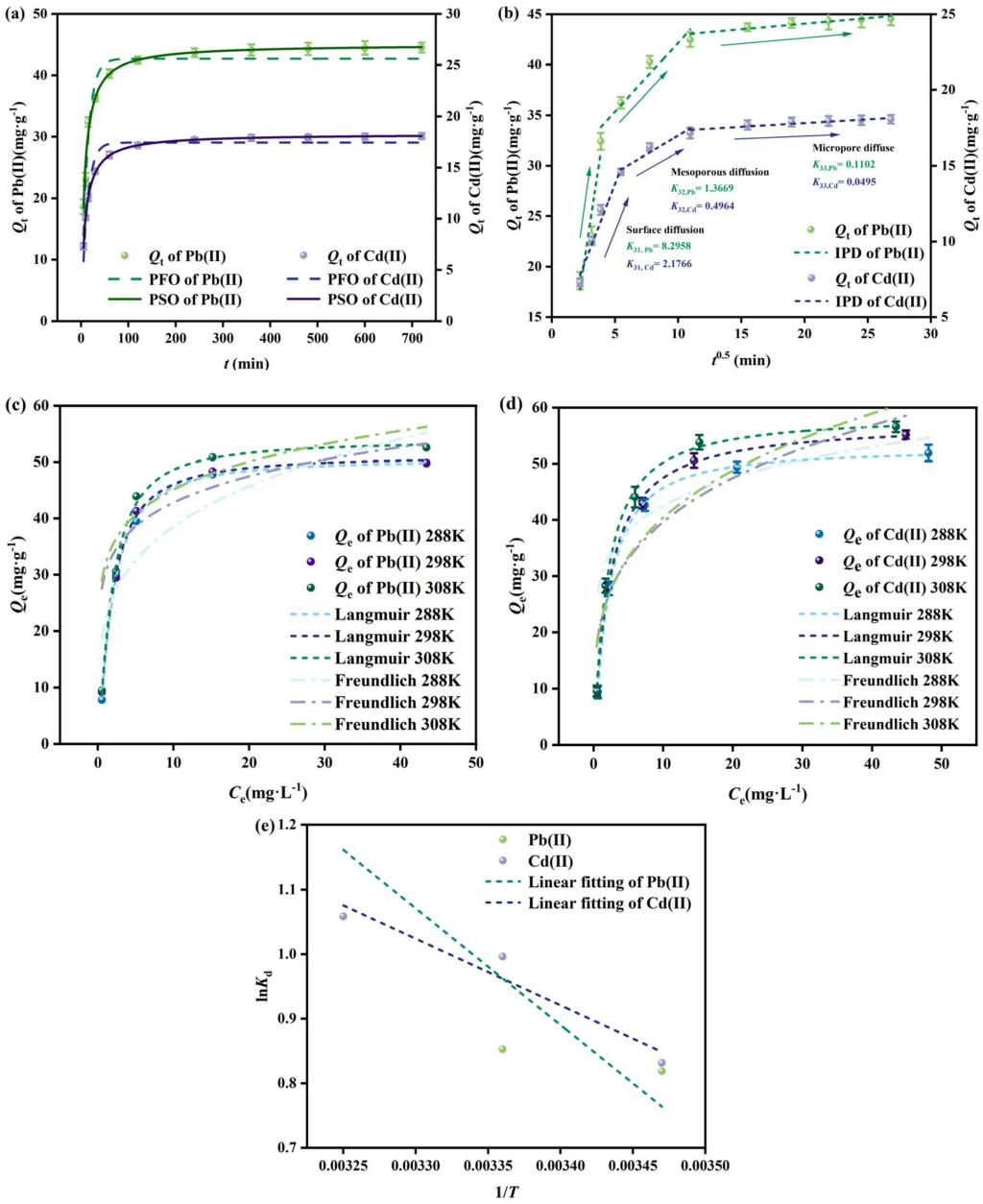


Figure 3. Adsorption characteristics of LBA. (**a**) PFO and PSO models for Pb(II) and Cd(II). (**b**) IPD models for Pb(II) and Cd(II). (**c**) Langmuir and Freundlich models for Pb(II). (**d**) Langmuir and Freundlich models for Cd(II). (**e**) Adsorption thermodynamics models for Pb(II) and Cd(II).

3.3.2. Adsorption Isotherm

The experimental results for the adsorption isotherms of Pb(II) and Cd(II) on LBA are shown in Table S3 and Figure 3c,d. Within the investigated temperature range (288 K~308 K), the Langmuir model provided significantly better fitting to the adsorption data (R^2 = 0.9943~0.9994) compared to the Freundlich model (R^2 = 0.7398~0.8551), indicating that the adsorption process conforms more closely to monolayer, homogeneous surface adsorption characteristics. According to the Langmuir theory, this result suggests that the active sites on the LBA surface are relatively uniformly distributed; adsorption primarily forms a monomolecular layer, and the adsorption sites are independent of each other without significant cooperative or repulsive interactions [44]. Further calculations revealed that the dimensionless separation factor RL values obtained from the Langmuir model all fell between 0.0199 and 0.1930 (<1), confirming that the adsorption process

is favorable and spontaneous under the experimental conditions [45]. Additionally, as temperature increased, the maximum Langmuir adsorption capacity Q_m continuously rose: Q_m for Pb(II) increased from 50.5679 mg·g^{-1} to 53.9296 mg·g^{-1}, and for Cd(II) from 52.7726 mg·g^{-1} to 58.6576 mg·g^{-1}, indicating that higher temperatures enhance adsorption capacity. This implies an endothermic nature for the adsorption process, possibly involving dehydration activation or overcoming energy barriers associated with interfacial bonding. To comprehensively evaluate the adsorption performance of LBA, Table S4 summarizes the maximum adsorption capacities of LBA toward Cd(II) and Pb(II) and previously reported bioadsorbents and biologically modified adsorbents. Biologically modified LBA exhibits a much higher adsorption capacity than raw lignite, confirming that white-rot fungus biotransformation effectively activates lignite. Although the xanthate-modified fungal adsorbent shows superior Cd(II) and Pb(II) uptake, its chemical modification reagent increases material cost. Some biochar materials possess a high Pb(II) adsorption capacity, but their preparation relies on high-temperature pyrolysis with significant energy consumption [46,47]. In contrast, the white-rot fungus modification of LBA proceeds under mild ambient conditions, representing a low-energy and environmentally friendly modification pathway.

3.3.3. Adsorption Thermodynamics

As shown in Table S5 and Figure 3e, all ΔG values are negative across the tested temperature range from 288 K to 308 K and become more negative as temperature rises. This finding demonstrates the spontaneous nature of the adsorption process, with greater thermodynamic spontaneity achieved at higher temperatures. Positive ΔH values are obtained for both target metal systems, verifying the endothermic feature of Pb(II) and Cd(II) adsorption onto LBA; accordingly, elevated temperatures facilitate the adsorption reaction. Positive ΔS values reflect increased disorder at the solid–liquid interface during adsorption, which may originate from the liberation of hydration water molecules surrounding heavy metal cations into the bulk solution. Collectively, the removal of Pb(II) and Cd(II) by LBA corresponds to a spontaneous, endothermic, entropy-favored adsorption process.

3.4. Adsorption Mechanism

3.4.1. XRD Analysis

Figure 4a shows the XRD characterization results for LBA, LBA-Pb(II), and LBA-Cd(II). The LBA sample exhibits characteristic diffraction peaks of SiO_2 (PDF# 46-1045) at approximately $2\theta = 20°$, 27°, and 50°, indicating that the LBA matrix is primarily composed of crystalline silica with amorphous components [48]. No diffraction signals corresponding to cadmium- or lead-containing phases were observed, confirming that LBA itself does not contain the target heavy metal elements. After adsorption of Pb(II) and Cd(II), the characteristic peaks of native SiO_2 in the LBA-Pb(II) and LBA-Cd(II) samples significantly weakened and were largely overlapped by numerous newly formed diffraction peaks, accompanied by multiple sets of characteristic signals attributable to insoluble cadmium- and lead-based crystalline phases, respectively. For the LBA-Cd(II) system, new diffraction peaks corresponding to $CdSO_4$ (PDF# 33-0049), CdO (PDF# 05-0640), Cd_3SiO_5 (PDF# 24-0237), and $Cd_2SO_4(OH)_2$ (PDF# 29-0256) were detected, whereas in the LBA-Pb(II) spectrum, characteristic peaks of $PbSO_4$ (PDF# 36-1461), PbO (PDF# 05-0570), $Pb_8Si_2O_{12}$ (PDF# 34-0516), and $Pb_2SO_4(OH)_2$ (PDF# 24-0579) were identified [49,50]. These observations indicate that SO_4^{2-} and OH^- in solution reacted with Cd(II)/Pb(II) to form precipitates, including metal sulfates, hydroxides, and basic sulfates [51]. The SO_4^{2-} originate from inherent organic sulfur and inorganic sulfur minerals in raw lignite. During biotransformation by white-rot fungi, sulfur-containing functional groups of lignite are

decomposed, releasing SO_4^{2-} and retaining it within the LBA solid matrix. Upon contact with Cd(II) and Pb(II), this intrinsic SO_4^{2-} participates in interfacial reactions to form metal sulfate and basic sulfate precipitates [52]. Furthermore, metal hydroxides can undergo dehydration to transform into metal oxides. Additionally, Cd(II) and Pb(II) reacted with SiO_2 in the LBA matrix via interfacial solid-state reactions, forming structurally stable metal silicate crystals. Therefore, the removal of Cd(II) and Pb(II) by LBA is achieved through a synergistic mechanism involving chemical precipitation and silicate-based interfacial solid-phase immobilization, ultimately converting heavy metals into various insoluble crystalline products for long-term stabilization [21].

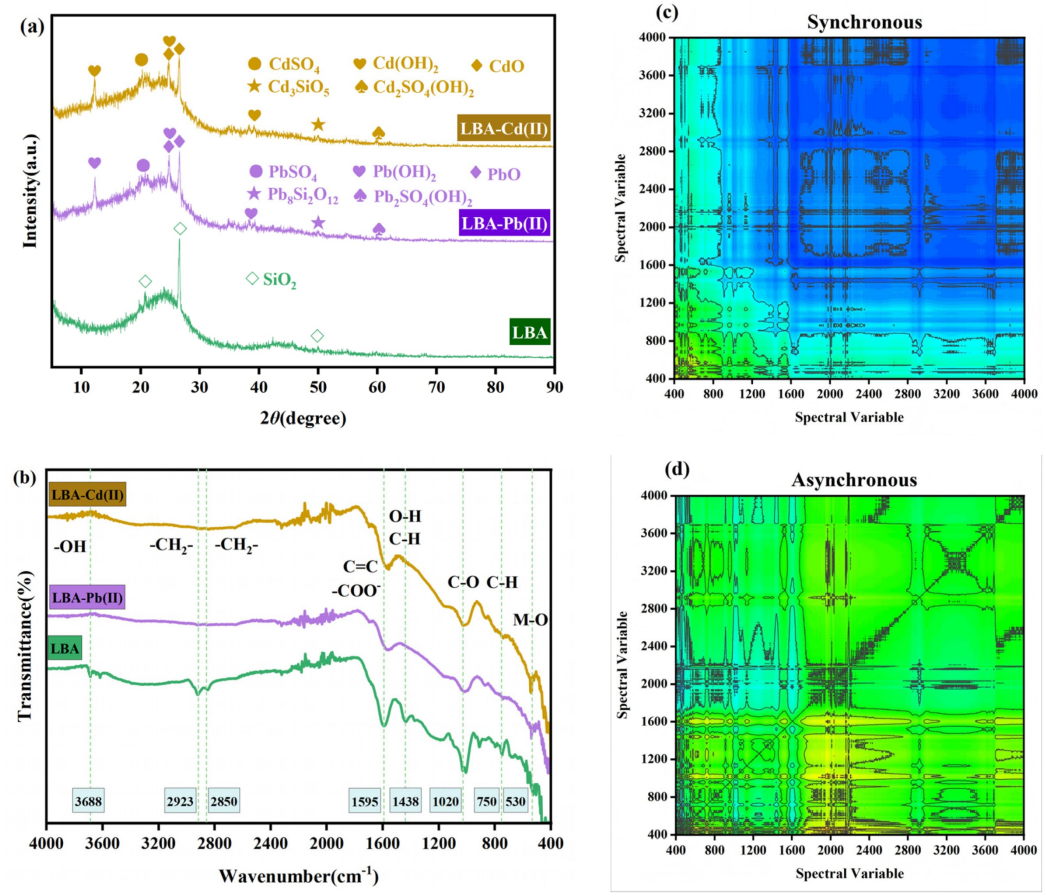


Figure 4. Microscopic characterization results for LBA after adsorption of Pb(II) and Cd(II). (**a**) XRD. (**b**) FTIR. (**c**) 2D-COS (synchronous). (**d**) 2D-COS (asynchronous).

3.4.2. FTIR Analysis

As shown in Figure 4b, the FTIR spectra of LBA before and after adsorption of Pb(II) and Cd(II) exhibit significant changes compared to the original spectrum, indicating recognizable alterations in the types, positions, and relative abundances of surface functional groups. Specifically: (1) The peak areas and intensities of characteristic peaks—such as free phenolic/alkanol hydroxyl groups (–OH, 3688 cm^{-1}), asymmetric C–H stretching vibration of methylene (–CH_2–) at 2923 cm^{-1}, symmetric C–H stretching vibration of methylene (–CH_2–) at 2850 cm^{-1}, and saturated C–H bending or in-plane O–H bending of phenolic hydroxyl groups at 1438 cm^{-1}—significantly decreased, suggesting that oxygen-containing and aliphatic functional groups participated in coordination. (2) The peak position shifted and intensity weakened for the overlapping bands of aromatic ring C=C skeletal stretching and asymmetric COO^- stretching vibrations of carboxylate at 1595 cm^{-1}, C–O single bond stretching at 1020 cm^{-1}, and out-of-plane bending vibrations of aromatic C–H at 750 cm^{-1},

reflecting changes in electron density of aromatic structures and oxygen-containing polar groups. (3) The intensity of the metal–oxygen bond (M–O) stretching vibration peak at 530 cm^{-1} increased, directly confirming the formation of coordination complexes between metal ions and oxygen-containing functional groups on the LBA surface. The FTIR analysis indicates that surface complexation occurred during the adsorption of Pb(II) and Cd(II) by LBA. Additionally, the weakening of the aromatic ring C=C characteristic peaks (around 1595 cm^{-1} and within the 1450~1600 cm^{-1} range) can be attributed to M-π coordination interactions formed between the π electrons of the aromatic ring acting as ligands and positively charged metal ions [32].

To gain deeper insight into the adsorption mechanism, the two-dimensional correlation spectroscopy (2D-COS) method was employed to determine the sequence in which surface functional groups participate in the adsorption process [53], using FTIR spectral data as the reference (Figure 4b). The order of functional group changes can be evaluated based on the signs of cross-peaks in the synchronous and asynchronous spectra (Figure 4c,d). In the synchronous map (Figure 4c), major auto-peaks appeared on the diagonal line. The positive cross-peaks of two bands showed that the variations in spectra occurred under the same orientation. An asynchronous map can represent the variance of spectral intensity (Figure 4d). Cross-peaks appeared at 1595, 1438, 1020, 750, and 530 cm^{-1} in the asynchronous map, and there were different phases between the dynamic spectral intensity changes in the two wavenumbers. These peaks on a nondiagonal line were positively–negatively correlated. The characteristics of auto-correlation and cross-correlation peaks in synchronous and asynchronous 2D correlation spectra can be explained by the Noda rules [54]. Table S6 shows the signs of cross-peaks for synchronous and asynchronous maps in LBA, along with their multiplication results. The order of peak vibrations before and after is 1020 cm^{-1} < 1595 cm^{-1} < 1438 cm^{-1} < 750 cm^{-1} < 530 cm^{-1}, indicating the sequence of functional groups involved in the adsorption processes of Pb(II) and Cd(II): C–O < –COO– < –OH < C–H < M–O.

3.4.3. XPS Analysis

Figure 5a–f show the XPS spectra of C 1s and O 1s for LBA before and after adsorption of Pb(II) and Cd(II). The C 1s spectrum can be deconvoluted into three main components with binding energies at 284.72 eV (C–C), 285.83 eV (C–O), and 289.78 eV (C=O), confirming that the LBA surface is rich in oxygen-containing functional groups. After adsorption of Pb(II) and Cd(II), the binding energies of all three carbon species shift positively, and their relative peak areas also show significant changes: the proportions of C–O and C=O components increase, while that of C–C decreases, indicating that oxygen-containing functional groups play a dominant role in the coordination process with metal ions [55]. Similarly, the O 1s spectrum can be fitted into three characteristic peaks at 530.2 eV (O^{2-}), 531.8 eV (C–OH/C–O–C), and 533.3 eV (O–H/C=O). After adsorption, the binding energies of all oxygen species generally increase, with the most pronounced shift observed in the C–OH/C–O–C peak. This suggests that oxygen atoms act as electron donors during coordination, leading to reduced electron cloud density and thus higher binding energy. This phenomenon aligns with the charge redistribution mechanism induced by metal–oxygen coordination [56]. Furthermore, distinct characteristic signals of Pb 4f and Cd 3d are clearly identified in the full XPS spectra of LBA-Pb(II) and LBA-Cd(II) samples (Figure 5g,h). The Pb 4f spectrum exhibits two peaks at 139.72 eV (Pb^{4+} in PbO_2) and 144.21 eV (Pb^{2+} in $PbCO_3$); the Cd 3d spectrum displays symmetric double peaks at 405.71 eV (Cd^{2+} in $CdCO_3$) and 412.37 eV (Cd^{2+} in CdO), confirming that the adsorbed Pb(II) and Cd(II) have transformed from free hydrated ions into stable metal oxide or carbonate precipitates, rather than elemental or zero-valent forms.

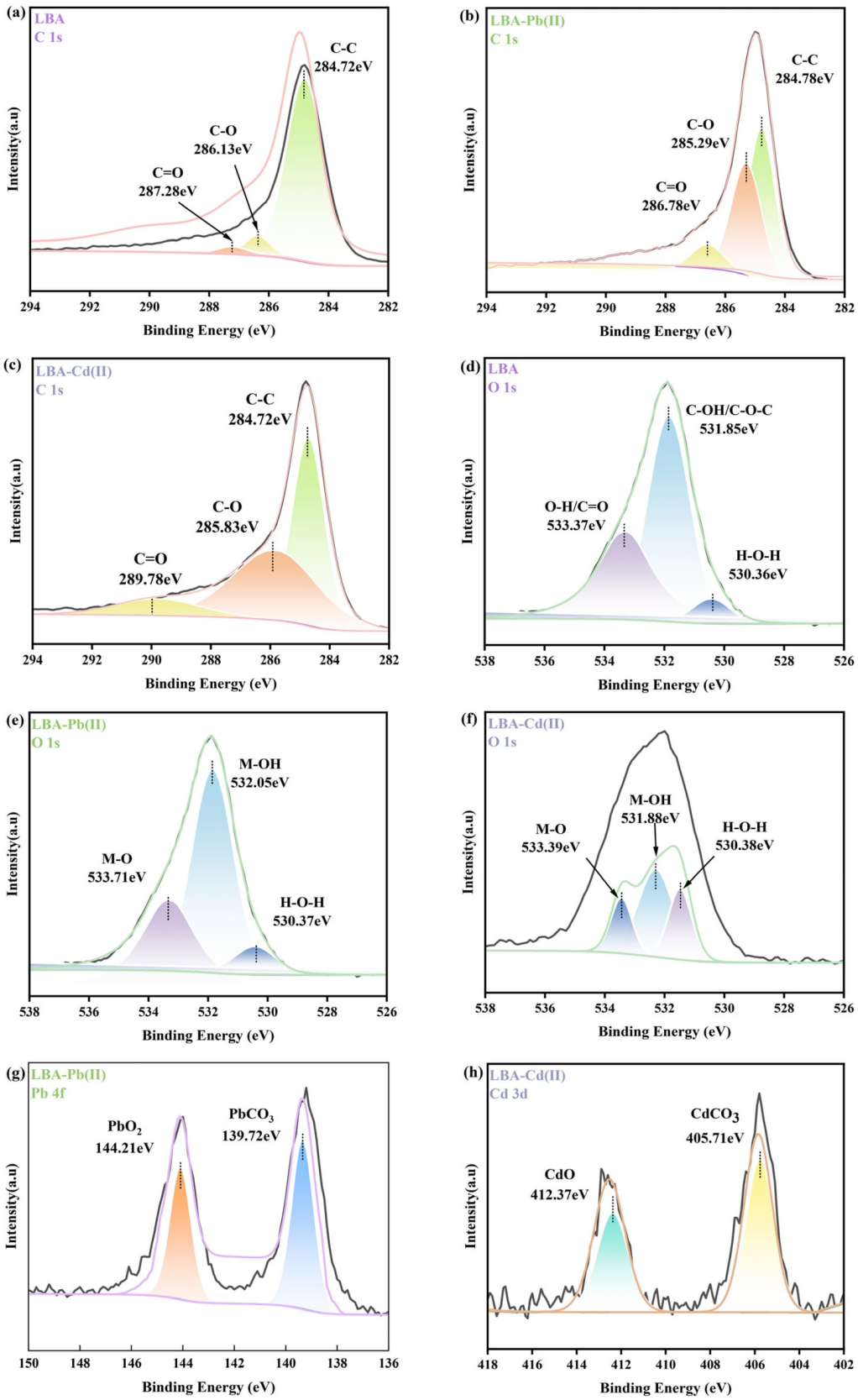


Figure 5. XPS results for LBA before and after adsorption of Pb(II) and Cd(II). (**a**) C 1s of LBA. (**b**) C 1s of LBA-Pb(II). (**c**) C 1s of LBA-Cd(II). (**d**) O 1s of LBA. (**e**) O 1s of LBA-Pb(II). (**f**) O 1s of LBA-Cd(II). (**g**) Pb 4f of LBA-Pb(II). (**h**) Cd 3d of LBA-Cd(II).

3.4.4. Contribution Rate of Different Mechanisms

The adsorption mechanisms of LBA for Pb(II) and Cd(II), as shown in Figure 6a, primarily include four processes: ion exchange, mineral precipitation, complexation with oxygen-containing functional groups, and π-electron coordination via aromatic structures. The quantitative contributions of each mechanism are presented in Figure 6b. Detailed analysis is as follows:

(1) Ion exchange (Q_e): Ionizable cations on the LBA surface (K^+, Na^+, Ca^{2+}, Mg^{2+}) undergo charge-equivalent replacement with Pb(II)/Cd(II) ions in solution. By measuring the concentration changes in these cations before and after adsorption using ICP-OES, the net release amount was calculated to determine the ion exchange contribution. At equilibrium, the ion exchange capacities for the Pb(II) and Cd(II) systems were 22.38 $mg \cdot g^{-1}$ and 18.45 $mg \cdot g^{-1}$, respectively, accounting for 17.25% and 16.87% of the total adsorption capacity of LBA, confirming that ion exchange is an important but non-dominant mechanism.

(2) Mineral precipitation (Q_p): CO_3^{2-} and OH^- in solution react with Pb(II)/Cd(II) to form insoluble carbonate, hydroxide, and basic salt crystals (e.g., $PbCO_3$ and $Cd(OH)_2$), thereby chemically immobilizing heavy metals. This process exhibits a coupling effect with ion exchange [57]. The contribution from mineral precipitation was determined by subtracting the adsorption capacities of demineralized organic matter (Q_a) and ion exchange (Q_e) from the total adsorption capacity; the adsorption capacities of demineralized organic matter were 70.83 $mg \cdot g^{-1}$ and 61.84 $mg \cdot g^{-1}$, respectively. Thus, the mineral precipitation capacities were calculated as 36.51 $mg \cdot g^{-1}$ and 29.08 $mg \cdot g^{-1}$, representing 28.14% and 26.59% of the total adsorption, respectively.

(3) Complexation with oxygen-containing functional groups (Q_f): Pb(II)/Cd(II) forms complexes with oxygen-containing groups such as –OH and –COOH on the LBA surface, accompanied by proton dissociation, which leads to a decrease in solution pH. The adsorption capacity associated with this mechanism was determined based on the change in pH before and after adsorption. The calculated Q_f values were 42.44 $mg \cdot g^{-1}$ and 36.27 $mg \cdot g^{-1}$, accounting for 32.72% and 33.16% of the total adsorption capacity, making it the dominant mechanism.

(4) π-electron coordination (Q_π): The π-electrons from graphitic/aromatic carbon structures in LBA act as ligands, forming M-π coordination complexes with Pb(II)/Cd(II). This contribution was indirectly quantified by comparing the adsorption differences between demineralized LBA (free of oxygen-containing functional group interference) and pristine LBA. The resulting Q_π values were 28.39 $mg \cdot g^{-1}$ and 25.57 $mg \cdot g^{-1}$, corresponding to 21.88% and 23.38% of the total adsorption capacity, respectively.

Overall, quantitative analysis indicates that the adsorption of Pb(II) and Cd(II) by LBA is predominantly governed by complexation with oxygen-containing functional groups (>32%), followed by mineral precipitation (~27%) and π-electron coordination (~23%), while ion exchange contributes the least (~17%).

3.5. Reutilization and Stability Analysis

Figure 7a shows the desorption efficiencies of five desorbing agents for Pb(II) and Cd(II) loaded on LBA material. The results indicate that both acidic and alkaline desorbing agents exhibit high desorption performance, while deionized water shows the lowest desorption rate. Specifically, 1.0 $mol \cdot L^{-1}$ HNO_3 achieved desorption rates of 73.23% and 69.48% for Pb(II) and Cd(II), respectively, whereas 1.0 $mol \cdot L^{-1}$ NaOH demonstrated the best desorption performance, with desorption rates reaching 88.12% and 84.36%, respectively. This phenomenon can be attributed to two distinct desorption mechanisms: under strong acidic conditions, high concentrations of H^+ compete with Pb(II)/Cd(II) for active sites on the LBA

surface, promoting metal ion detachment; under strong alkaline conditions, OH^- not only induces the formation of insoluble hydroxide precipitates (e.g., $Pb(OH)_2$, $Cd(OH)_2$) but also forms soluble hydroxyl complexes (e.g., $[Pb(OH)_4]^{2-}$ and $[Pb_3(OH)_4]^{2+}$), significantly reducing the thermodynamic stability of metal ions in the solid phase and thereby enhancing the driving force for desorption. Figure 7b shows the regeneration performance of LBA under a 1.0 mol·L^{-1} NaOH system after five consecutive adsorption–desorption cycles. During the first three cycles, the removal efficiencies of Pb(II) and Cd(II) by LBA remained above 70%, with corresponding adsorption capacities of 23.5975 mg·g-1 and 5.7870 mg·g^{-1}, indicating the good initial regeneration stability of the material. To evaluate the practical application potential of LBA, adsorption experiments were further conducted using real automotive paint wastewater. As shown in Figure 7c, LBA achieved removal efficiencies exceeding 83% for Pb(II), Cd(II), Fe(II), Mn(II), Cu(II), and Zn(II) in the wastewater, confirming its strong heavy metal capture capability even in complex matrices. However, compared to simulated single or binary systems, the removal rates for each metal generally decreased by 5~12%, primarily due to competitive adsorption among coexisting ions in actual wastewater, as well as the shielding or occupation of adsorption sites by non-target components such as organic additives, suspended particles, and chelating agents.

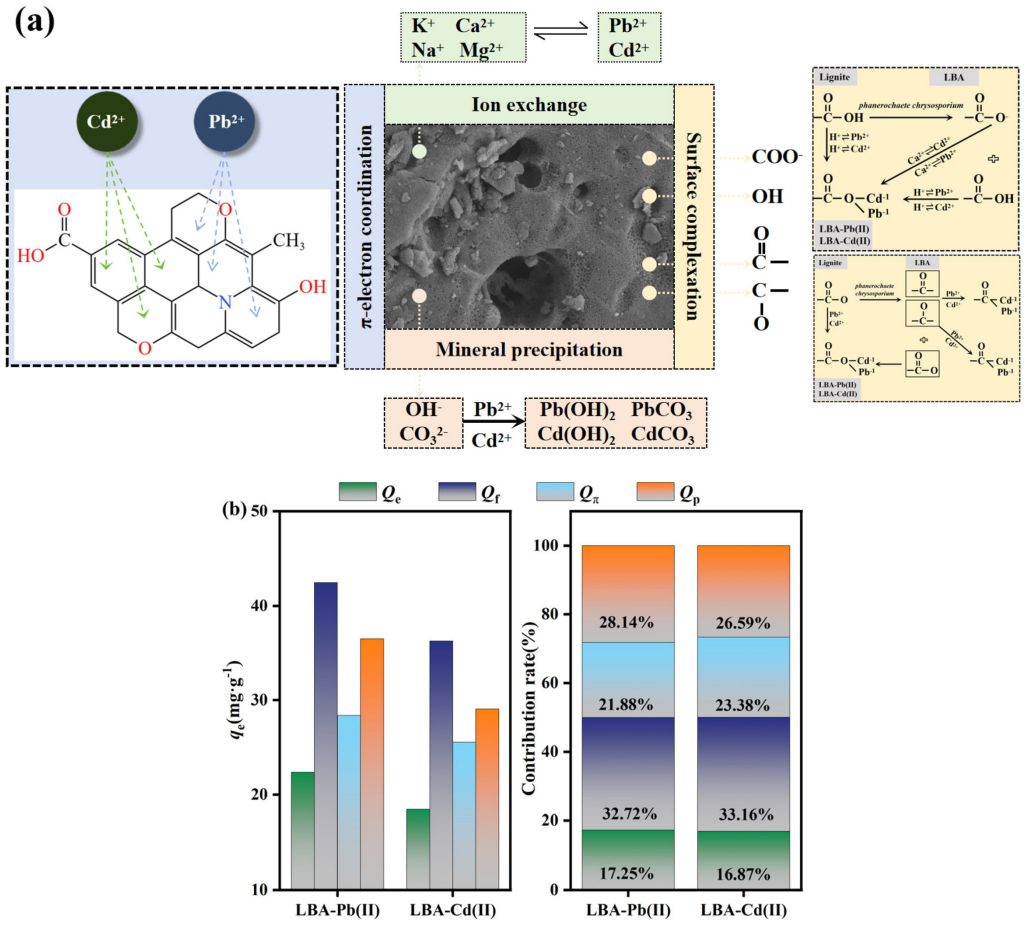


Figure 6. Adsorption mechanism of Pb(II) and Cd(II) in solution for LBA. (**a**) Adsorption mechanism. (**b**) Contribution of each mechanism.

It should be noted that although the regeneration performance of LBA is verified in laboratory-scale desorption–adsorption cycles, practical engineering application still faces challenges. The high-concentration heavy metal-containing desorption effluent needs fur-

ther proper disposal. The downstream treatment of desorption wastewater is not explored in this work, which will be considered in our follow-up research.

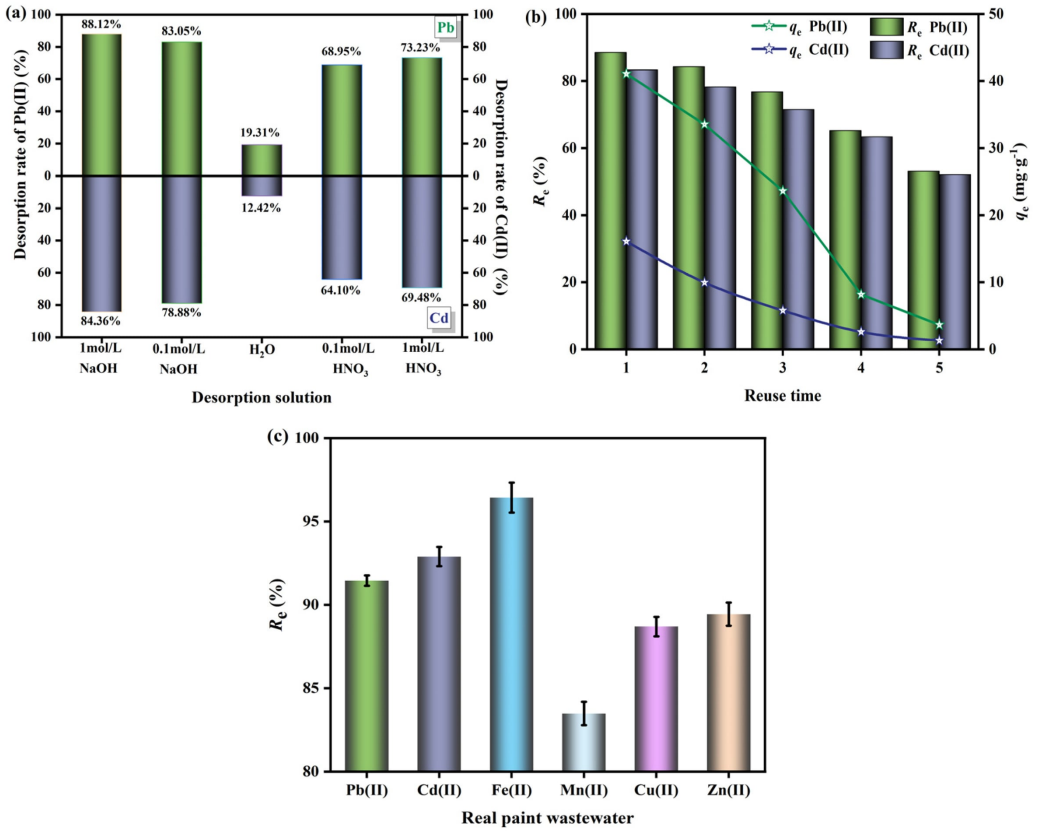


Figure 7. Reutilization and stability of LBA. (**a**) Adsorption–desorption. (**b**) Recycling and reuse. (**c**) Application of actual paint wastewater.

4. Conclusions

We successfully utilized *Phanerochaete chrysosporium* to biologically modify low-calorific lignite, producing a novel lignite-based adsorbent (LBA) for the efficient removal of heavy metal ions Pb(II) and Cd(II) from wastewater. The optimal process parameters for LBA treatment of lead- and cadmium-containing wastewater were systematically determined: the optimal dosages for Pb(II) and Cd(II) were 0.4 g·L^{-1} and 1.3 g·L^{-1}, respectively. Under weakly acidic conditions (pH 4~6) and typical environmental concentrations (Pb(II): 10 mg·L^{-1}; Cd(II): 3 mg·L^{-1}), both removal efficiency and equilibrium adsorption capacity reached their peak values. Kinetic and isotherm fitting results indicated that the adsorption process was primarily governed by chemical adsorption, showing excellent agreement with the pseudo-second-order kinetic model and the Langmuir monolayer adsorption isotherm model. The calculated maximum saturated adsorption capacities were 51.20 mg·g^{-1} for Pb(II) and 57.34 mg·g^{-1} for Cd(II), confirming that *Phanerochaete chrysosporium* modification significantly enhanced the surface activity and heavy metal binding capacity of low-calorific lignite. Mechanistic analysis revealed that the removal of Pb(II) and Cd(II) by LBA was driven synergistically by four mechanisms: complexation with oxygen-containing functional groups, mineral precipitation, π-electron coordination, and ion exchange. Among these, complexation with oxygen-containing groups dominated (32.6%), followed by mineral precipitation (27.1%), π-electron coordination (23.4%), and ion exchange (16.9%). After three adsorption–desorption cycles, LBA maintained removal efficiencies above 70% for both Pb(II) and Cd(II), demonstrating excellent structural stability and regenerability. In

real automotive paint wastewater, LBA achieved removal rates exceeding 83% for Pb(II), Cd(II), Cu(II), Zn(II), Fe(II), and Mn(II), verifying its strong adaptability in complex industrial effluents with high ionic strength and multiple coexisting components. This study not only enables the functional utilization of low-calorific brown coal but also develops a new heavy metal remediation material that combines high efficiency, regenerability, and practical feasibility, providing a reliable technical pathway and theoretical foundation for treating lead- and cadmium-contaminated wastewater.

Supplementary Materials: The following supporting information can be downloaded at https://www.mdpi.com/article/10.3390/w18212700/s1: Text S1: The corresponding mathematical expressions of adsorption kinetics and adsorption isotherms. Table S1: Summary of parameters for the batch adsorption experiments. Table S2: The adsorption kinetics parameters of LBA for Pb(II) and Cd(II). Table S3: The adsorption isotherm parameters of LBA for Pb(II) and Cd(II). Table S4: Comparison of maximum adsorption capacities of LBA and other reported adsorbents for Cd(II) and Pb(II) removal. Table S5: The adsorption thermodynamic parameters of LBA for Pb(II), and Cd(II). Table S6: Cross peak symbols for synchronous and asynchronous spectral and their multiplication results in LBA. Figure S1. Schematic diagram of the synthesis procedures of LBA.

Author Contributions: Conceptualization, W.A.; methodology, W.A. and H.C.; software, X.C. and G.F.; investigation, T.W.; resources, Q.W.; data curation, B.X.; writing—original draft preparation, W.A. and H.C.; writing—review and editing, W.A.; funding acquisition, W.A. All authors have read and agreed to the published version of the manuscript.

Funding: This research was funded by the Education Department of Hainan Province (Hnjg2026ZC-157) and the Basic Scientific Research Project of the Liaoning Provincial Department of Education (JYTMS20230791).

Data Availability Statement: All data generated or analyzed during this study are included in this published article and its Supplementary Materials. Further inquiries can be directed to the corresponding author.

Conflicts of Interest: The authors declare no conflicts of interest.

References

1. Carvalho, S.; Eusébio, M.; Velizarov, S. Techno-Economic and Feasibility Assessment of Membrane-Based Wastewater Treatment and Reuse in the Automotive Industry. *Separations* **2025**, *12*, 30. [CrossRef]
2. Yavuz, G.; Okumus, M.B.; Bostanci, S.; Karadirek, I.E.; Ciggin, A.S. Feasibility of Fenton-based oxidation for reducing organic content, toxicity, and carbon footprint of automotive industry wastewater. *Int. J. Environ. Sci. Technol.* **2025**, *22*, 12547–12565. [CrossRef]
3. Akpomie, K.G.; Dawodu, F.A. Treatment of an automobile effluent from heavy metals contamination by an eco-friendly montmorillonite. *J. Adv. Res.* **2015**, *6*, 1003–1013. [CrossRef]
4. Wang, Y.L.; Zeng, W.B.; Wan, X.M.; Wang, L.; Lei, M.; Chen, T.B. Modeling the removal of Cd(II) and Pb(II) from aqueous solutions by biochar derived from arsenic hyperaccumulator Pteris vittata. *J. Environ. Manag.* **2025**, *381*, 125280. [CrossRef]
5. Zhang, H.; Huang, H.Y.; Fang, Y.R.; Cai, J.M.; Lv, X.Y.; Wu, W.L.; Gu, Q.; Qian, R.; Yu, K.R.; Tang, K.H.D.; et al. Synthesis of magnetic biochar co-doped with sulfur, iron, and manganese via a novel modification method for simultaneous Cd and Pb remediation. *Sep. Purif. Technol.* **2025**, *363*, 132025. [CrossRef]
6. Zhang, G.J.; Liu, S.W.; Sun, Q.H.; Sun, J.; Tian, N.; Wu, Z.F.; Jiang, L. A multi-level porous MgO/biochar composite for the highly efficient adsorption of Pb(II) and Cd(II) from water. *New Carbon Mater.* **2026**, *41*, 675–692. [CrossRef]
7. Hao, P.X.; Fu, H.C.; Ma, S.L.; Xue, W.J.; Xiong, S.W.; Li, G.X.; Duan, R.; Sui, F.Q.; Li, C.; Zhao, P. MgO-embedded S-doped porous biochar composites for efficient removal Cd(II) and Pb(II) in water: DFT studies and mechanistic insights. *Sep. Purif. Technol.* **2025**, *363*, 132079. [CrossRef]
8. Huang, Z.Q.; Wang, Q.; Zhang, Y.F.; Du, B.Y.; Zhou, J.; Ji, D.L. Effects of Pyrolysis Temperatures and Modified Methods on Rice Husk-Derived Biochar Characteristics and Heavy Metal Adsorption. *Molecules* **2025**, *30*, 3616. [CrossRef]
9. Wei, T.; Wang, Y.Y.; Ma, X.L.; Hu, R.Y.; Guo, J.K.; Hua, L.; Zhang, X.K. Bacteria-loaded Biochar (BC)/Phosphorus-Modified Biochar (PBC): An Efficient Biosorbent for Remediation of Cd and Pb Co-Contaminated Soil. *Water Air Soil Pollut.* **2025**, *236*, 979. [CrossRef]

10. Zhao, Y.; Yao, J.; Min, N.; Ma, B.; Chai, W.P.; Ma, Y. Efficient removal of Cu^{2+}, Pb^{2+}, and Cd^{2+} by two magnetic biochar-montmorillonite composites and the application in synthetic wastewater. *Sep. Purif. Technol.* **2026**, *391*, 136996. [CrossRef]
11. Ren, S.H.; Luo, Z.Y.; Pan, Y.W.; Ling, C.; Yu, L.; Yin, K. Distinctive adsorption and desorption behaviors of temporal and post-treatment heavy metals by iron nanoparticles in the presence of microplastics. *Sci. Total Environ.* **2023**, *878*, 163141. [CrossRef]
12. Kim, S.H.; Park, J.I.; Lee, S.; Kim, H.; Son, B.; Seo, J.; Kim, C.; Jeong, Y.; Choi, K.; Jeong, S.; et al. Enhancing adsorption efficiency for environmentally-friendly removal of As(V) and Pb(II) using a biochar-iron oxide composite. *Appl. Surf. Sci.* **2024**, *667*, 160348. [CrossRef]
13. Yang, W.; Wen, J.; Zhou, Y.C.; Cheng, W.X.; Zheng, Y.L. Simultaneous removal of cadmium and arsenic co-contamination by iron/sulfur-modified zeolites combined with sulfate-reducing bacteria. *J. Water Process Eng.* **2024**, *67*, 106236. [CrossRef]
14. An, W.B.; Liu, Y.F.; Chen, H.; Sun, X.Y.; Wang, Q.Q.; Hu, X.C.; Di, J.Z. Adsorption properties of Pb(II) and Cd(II) in acid mine drainage by oyster shell loaded lignite composite in different morphologies. *Sci. Rep.* **2024**, *14*, 11627. [CrossRef]
15. Cao, B.; Qu, J.H.; Yuan, Y.H.; Zhang, W.H.; Miao, X.M.; Zhang, X.R.; Xu, Y.; Han, T.Y.; Song, H.J.; Ma, S.Y.; et al. Efficient scavenging of aqueous Pb(II)/Cd(II) by sulfide-iron decorated biochar: Performance, mechanisms and reusability exploration. *J. Environ. Chem. Eng.* **2022**, *10*, 107531. [CrossRef]
16. Abidli, A.; Ben Rejeb, Z.; Zaoui, A.; Naguib, H.E.; Park, C.B. Comprehensive insights into the application of graphene-based aerogels for metals removal from aqueous media: Surface chemistry, mechanisms, and key features. *Adv. Colloid Interface Sci.* **2024**, *335*, 103338. [CrossRef]
17. Mlayah, A.; Jellali, S.; Azzaz, A.A.; Jeguirim, M.; Sellalmi, H.; Hamdi, N. Investigations on lignite use for lead removal from aqueous solutions under static and dynamic conditions: Adsorption properties and mechanism exploration. *Comptes Rendus Chim.* **2021**, *24*, 7–22. [CrossRef]
18. Hu, K.; Liu, A.; Li, R.; Zheng, R.; Liu, C.; Ali, M. H2 adsorption on coal considering the nanopore size distribution: Insight from the lattice density functional theory. *J. Energy Storage* **2026**, *182*, 124540. [CrossRef]
19. Jellali, S.; Azzaz, A.A.; Jeguirim, M.; Hamdi, H.; Mlayah, A. Use of lignite as a low-cost material for cadmium and copper removal from aqueous solutions: Assessment of adsorption characteristics and exploration of involved mechanisms. *Water* **2021**, *13*, 164. [CrossRef]
20. Huang, B.; Liu, G.W.; Wang, P.H.; Zhao, X.; Xu, H.X. Effect of nitric acid modification on characteristics and adsorption properties of lignite. *Processes* **2019**, *7*, 167. [CrossRef]
21. Wang, P.; Huang, Z.B.; Fu, Z.Y.; Zhao, P.; Feng, Z.S.; Wang, Y.; Li, F.Z. Adsorption mechanism of Cd(II) by calcium-modified lignite-derived humin in aqueous solutions. *Int. J. Coal Sci. Technol.* **2022**, *9*, 37. [CrossRef]
22. Sekhohola-Dlamini, L.M.; Khan, S.; Wang, B.B.; Yu, Z.S.; Cowan, A.K. Recent progress on the biological degradation and solubilization of coal. *Biodegradation* **2025**, *36*, 84. [CrossRef]
23. Zhao, Y.L.; Chai, R.N.; Duan, J.G.; Yang, Z.Y.; Zhang, S.H.; Liu, Y.Y.; Wang, X.X.; Cheng, J.G. Isolation of native microorganisms from Shengli lignite and study on their ability to dissolve lignite. *Bioprocess Biosyst. Eng.* **2024**, *47*, 1985–1997. [CrossRef]
24. Shi, C.; Liu, X.R.; Zhao, S.S.; Yang, Z.W.; Lu, X.; Tong, M. Sequential degradations of Dananhu lignites by Nocardia mangyaensis and Bacillus licheniformis. *Fuel* **2022**, *318*, 123623. [CrossRef]
25. Wang, Y.Y.; Cao, W.L.; Zhu, T.Y.; Li, J.X.; Nussipov, D.; Tastambek, K.; Liu, X.R. The mechanism underlying lignite biodegradation by Cupriavidus sp isolated from sludge. *Biodegradation* **2025**, *36*, 98. [CrossRef]
26. Wang, Y.Y.; Cao, W.L.; Nussipov, D.; Bao, Y.; Li, J.X.; Shi, Z.W.; Zhou, A.N.; Tastambek, K.; Liu, X.R. Comparative biodegradation of lignite by Bacillus cereus and Lelliottia amnigena: Elucidating enzymatic, adhesion, and metabolic mechanisms through multi-technique analysis. *Process Biochem.* **2026**, *161*, 249–260. [CrossRef]
27. Klein, O.I.; Kulikova, N.A.; Stepanova, E.V.; Filippova, O.I.; Fedorova, T.V.; Maloshenok, L.G.; Filimonov, I.S.; Koroleva, O.V. Preparation and characterization of bioactive products obtained via the solubilization of brown coal by white rot fungi. *Appl. Biochem. Microbiol.* **2014**, *50*, 730–736. [CrossRef]
28. Yin, S.D.; Tao, X.X.; Shi, K.Y.; Tan, Z.C. Biosolubilisation of chinese lignite. *Energy* **2009**, *34*, 775–781. [CrossRef]
29. Wang, Y.H.; Chen, G.H.; Wang, Y.Y.; Yu, D.S.; Gong, Y.H.; Yao, T.T.; Shan, Y. Optimizing Nutrient Cycling in Organic Waste Composting: Role of SSP and Phanerochaete chrysosporium in Mitigating Nitrogen Loss and Efficient Lignocellulose Degradation. *Water Environ. Res.* **2025**, *97*, e70154. [CrossRef]
30. Zhai, S.M.; Wang, K.; Yu, F.C.; Gao, Z.L.; Yang, X.; Cao, X.Q.; Shaghaleh, H.; Hamoud, Y.A. Effects of Trichoderma harzianum combined with Phanerochaete chrysosporium on lignin degradation and humification during chicken manure and rice husk composting. *Front. Microbiol.* **2025**, *16*, 1515931. [CrossRef]
31. Zhu, J.; Jin, J.; Ju, L.; Xia, Y.; Zou, Y.; Yang, H.; Xu, R. WSO-SVM-based optimization of low-carbon composite flocculant and its microstructural mechanism for engineering waste slurry dewatering. *Can. Geotech. J.* **2026**, *63*, 1–25. [CrossRef]
32. Ma, W.C.; Han, R.; Zhang, W.; Zhang, H.; Chen, L.; Zhu, L. Magnetic biochar enhanced copper immobilization in agricultural lands: Insights from adsorption precipitation and redox. *J. Environ. Manag.* **2024**, *352*, 120058. [CrossRef]

33. Cui, X.Q.; Hao, H.L.; Zhang, C.K.; He, Z.L.; Yang, X.E. Capacity and mechanisms of ammonium and cadmium sorption on different wetland-plant derived biochars. *Sci. Total Environ.* **2016**, *539*, 566–575. [CrossRef]
34. Thommes, M.; Kaneko, K.; Neimark, A.V.; Olivier, J.P.; Rodriguez-Reinoso, F.; Rouquerol, J.; Sing, K.S.W. Physisorption of gases, with special reference to the evaluation of surface area and pore size distribution (IUPAC Technical Report). *Pure Appl. Chem.* **2015**, *87*, 1051–1069. [CrossRef]
35. Wang, Z.Y.; Cheng, Y.P.; Wang, G.; Ni, G.H.; Wang, L. Comparative analysis of pore structure parameters of coal by using low pressure argon and nitrogen adsorption. *Fuel* **2022**, *309*, 122120. [CrossRef]
36. De Souza, E.C.; Pimenta, A.S.; Da Silva, A.J.F.; Do Nascimento, P.F.P.; Ighalo, J.O. Oxidized eucalyptus charcoal: A renewable biosorbent for removing heavy metals from aqueous solutions. *Biomass Convers. Biorefin.* **2023**, *13*, 4105–4119. [CrossRef]
37. Wu, J.Z.; Huang, D.; Liu, X.M.; Meng, J.; Tang, C.X.; Xu, J.M. Remediation of As(III) and Cd(II) co-contamination and its mechanism in aqueous systems by a novel calcium-based magnetic biochar. *J. Hazard. Mater.* **2018**, *348*, 10–19. [CrossRef]
38. Eletta, O.A.A.; Ayandele, F.O.; Ighalo, J.O. Adsorption of Pb(II) and Fe(II) by mesoporous composite activated carbon from Tithonia diversifolia stalk and Theobroma cacao pod. *Biomass Convers. Biorefin.* **2023**, *13*, 9831–9840. [CrossRef]
39. Ramirez Arenas, L.R.; Le Coustumer, P.; Ramseier Gentile, S.R.; Zimmermann, S.; Stoll, S. Removal efficiency and adsorption mechanisms of CeO2 nanoparticles onto granular activated carbon used in drinking water treatment plants. *Sci. Total Environ.* **2023**, *856*, 159261. [CrossRef]
40. Ni, B.J.; Huang, Q.S.; Wang, C.; Ni, T.Y.; Sun, J.; Wei, W. Competitive adsorption of heavy metals in aqueous solution onto biochar derived from anaerobically digested sludge. *Chemosphere* **2019**, *219*, 351–357. [CrossRef]
41. Albadarin, A.B.; Mangwandi, C.; Al-Muhtaseb, A.H.; Walker, G.M.; Allen, S.J.; Ahmad, M.N.M. Kinetic and thermodynamics of chromium ions adsorption onto low-cost dolomite adsorbent. *Chem. Eng. J.* **2012**, *179*, 193–202. [CrossRef]
42. Feng, G.R.; Ma, J.C.; Zhang, X.P.; Zhang, Q.F.; Xiao, Y.Q.; Ma, Q.L.; Wang, S.B. Magnetic natural composite Fe3O4-chitosan@bentonite for removal of heavy metals from acid mine drainage. *J. Colloid Interface Sci.* **2019**, *538*, 132–141. [CrossRef]
43. Liang, Q.W.; Luo, H.J.; Geng, J.J.; Chen, J.D. Facile one-pot preparation of nitrogen-doped ultra-light graphene oxide aerogel and its prominent adsorption performance of Cr(VI). *Chem. Eng. J.* **2018**, *338*, 62–71. [CrossRef]
44. Li, K.G.; Xu, W.J.; Song, H.J.; Bi, F.X.; Li, Y.H.; Jiang, Z.; Tao, Y.; Qu, J.H.; Zhang, Y. Superior reduction and immobilization of Cr(VI) in soil utilizing sulfide nanoscale zero-valent iron supported by phosphoric acid-modified biochar: Efficiency and mechanism investigation. *Sci. Total Environ.* **2024**, *907*, 168133. [CrossRef]
45. Dehghani, M.H.; Yetilmezsoy, K.; Salari, M.; Heidarinejad, Z.; Yousefi, M.; Sillanpää, M. Adsorptive removal of cobalt(II) from aqueous solutions using multi-walled carbon nanotubes and γ-alumina as novel adsorbents: Modelling and optimization based on response surface methodology and artificial neural network. *J. Mol. Liq.* **2020**, *299*, 112154. [CrossRef]
46. Cheng, J.G.; Zhang, S.F.; Fang, C.; Ma, L.T.; Duan, J.G.; Fang, X.; Li, R.H. Removal of Heavy Metal Ions from Aqueous Solution Using Biotransformed Lignite. *Molecules* **2023**, *28*, 5031. [CrossRef]
47. Wang, C.X.; Chen, Z.R.; Wang, N.N.; Wang, J.Q.; He, R.S.; Chen, Y.; Nuhu, H.; Chen, H.; Lin, Z.X.; Fan, M.Q.; et al. Sponge-like Modified White-Rot Fungi Adsorbent for Rapid Removal of Pb(II) and Cd(II) from Solution: Selective Performance and Mechanistic Insights. *Separations* **2025**, *12*, 172. [CrossRef]
48. Bartczak, P.; Norman, M.; Klapiszewski, L.; Karwanska, N.; Kawalec, M.; Baczynska, M.; Wysokowski, M.; Zdarta, J.; Ciesielczyk, F.; Jesionowski, T. Removal of nickel(II) and lead(II) ions from aqueous solution using peat as a low-cost adsorbent: A kinetic and equilibrium study. *Arab. J. Chem.* **2018**, *11*, 1209–1222. [CrossRef]
49. Roza-Llera, A.; Di Lorenzo, F.; Churakov, S.V.; Jiménez, A.; Fernández-Díaz, L. Pb Removal Efficiency by Calcium Carbonates: Biogenic versus Abiogenic Materials. *Cryst. Growth Des.* **2024**, *24*, 79–92. [CrossRef]
50. Chen, Q.Y.Y.; Min, Q.; Wu, H.; Zhang, L.; Si, Y.B. Biomineralization of Cd^{2+} and Pb^{2+} by sulfate-reducing bacteria Desulfovibrio desulfuricans and Desulfobulbus propionicus. *Front. Environ. Sci.* **2025**, *13*, 1591564. [CrossRef]
51. Hao, L.P.; Gao, W.Y.; Yan, S.; Niu, M.H.; Liu, G.S.; Hao, H.S. Preparation and characterization of porous ceramics with low-grade diatomite and oyster shell. *Mater. Chem. Phys.* **2019**, *235*, 121741. [CrossRef]
52. He, H.; Cao, M.J.; Zhan, D.; Xia, W.C.; Chen, S.J.; Tao, X.X.; Huang, Z.X. Preliminary Study on the Surface Modification of Lignite and Bioflotation by White-Rot Fungi Hypocrea lixii AH. *Minerals* **2023**, *13*, 1492. [CrossRef]
53. Lasch, P.; Noda, I. Two-Dimensional Correlation Spectroscopy (2D-COS) for Analysis of Spatially Resolved Vibrational Spectra. *Appl. Spectrosc.* **2019**, *73*, 359–379. [CrossRef]
54. An, W.; Wang, Q.; Chen, H.; Liu, Y.; Hu, X.; Di, J. Efficient Recovery of Phosphate from Water Media by Iron-Magnesium Functionalized Lignite: Adsorption Evaluation, Mechanism Revelation and Potential Application Exploration. *Molecules* **2024**, *29*, 1252. [CrossRef]
55. Zeng, T.T.; Liu, J.Y.; Chen, Y.Q.; Naz, A.; Su, M.H.; Liu, Z.; Chen, D.Y.; Hou, L.A. Development of an eco-friendly Bacillus amyloliquefaciens doped biochar for efficient U(VI) removal from water and insights into its adsorption mechanism. *Environ. Technol. Innov.* **2025**, *40*, 104492. [CrossRef]

56. Babeker, T.M.A.; Khalil, M.N.; Fayad, E.; Alshaya, D.S.; Elsaid, F.G.; Elhassan, I.A. Superior Cu (II) purification using carrageenan biochar-olivine composite: Synergistic effects of K (I), Mg (II), Fe (II/ III), and Si (IV). *Environ. Res.* **2025**, *285*, 122282. [CrossRef]
57. Li, X.L.; Deng, H.Y.; Zhou, J.; Touqeer, A.; Li, W.B. Adsorption mechanism of Cu(II) and Pb(II) by starch biochar co-modified with plant extract and chitosan. *Int. J. Biol. Macromol.* **2025**, *320*, 145971. [CrossRef]

Disclaimer/Publisher's Note: The statements, opinions and data contained in all publications are solely those of the individual author(s) and contributor(s) and not of MDPI and/or the editor(s). MDPI and/or the editor(s) disclaim responsibility for any injury to people or property resulting from any ideas, methods, instructions or products referred to in the content.